Domain wall motion by localized temperature gradients

Simone Moretti,* Victor Raposo, Eduardo Martinez, and Luis Lopez-Diaz
Department of Applied Physics, University of Salamanca, Plaza de los Caidos, Salamanca 37008, Spain
(Received 25 November 2016; revised manuscript received 30 January 2017; published 21 February 2017)

Magnetic domain wall (DW) motion induced by a localized Gaussian temperature profile is studied in a Permalloy nanostrip within the framework of the stochastic Landau-Lifshitz-Bloch equation. The different contributions to thermally induced DW motion, entropic torque and magnonic spin transfer torque, are isolated and compared. The analysis of magnonic spin transfer torque includes a description of thermally excited magnons in the sample. A third driving force due to a thermally induced dipolar field is found and described. Finally, thermally induced DW motion is studied under realistic conditions by taking into account the edge roughness. The results give quantitative insights into the different mechanisms responsible for domain wall motion in temperature gradients and allow for comparison with experimental results.

DOI: 10.1103/PhysRevB.95.064419

I. INTRODUCTION

Controlling magnetic domain walls (DWs) in ferromagnetic (FM) and antiferromagnetic (AFM) nanostructures has recently attracted considerable interest due to its potential for new logic [1] and memory devices [2] and for the very rich physics involved. In fact, DWs can be moved by several means such as external magnetic fields [3], spin-polarized currents [4–7], and spin waves [8–11]. A new interesting option is the motion of DWs by thermal gradients (TGs), which was recently observed in a few experiments on FM conductors [12,13], semiconductors [14], and insulators [15]. Spin caloritronics [16] is a new emerging subfield of spintronics which aims to understand such complex interaction between heat, charge, and spin transport. One of the interesting features of thermally induced DW motion is its applicability to FM insulators and AFM [17]. Furthermore, since it does not imply charge transport and related Joule heating, it would avoid energy dissipation in FM conductors, or it might represent a solution for harvesting the heat dissipated in electronic circuits [16,18].

From a theoretical point of view, it is known that thermally induced DW motion has at least two main causes: (1) the so-called entropic torque (ET) [19–21], which drives the DW towards the hot region due to maximization (minimization) of entropy (free energy), and (2) the magnonic spin transfer torque (μSTT) [10,21,22] due to the interaction between thermal magnons, propagating from the hot to the cold region, and the DW. While the entropic torque always drives the DW towards the hotter region [19–21,23] (the DW energy is always lower where the temperature is higher), the μSTT can drive the DW towards either the hot or the cold part depending on the magnons' behavior [9]: if magnons are transmitted through the DW, then angular momentum transfer leads to DW motion towards the hot part (opposite the direction of magnon propagation), as predicted in Refs. [10,21,22]. On the other hand, if magnons are reflected, linear momentum transfer leads to DW motion towards the cold part (the same direction as magnon propagation), as shown in Refs. [8,24,25]. Moreover, magnon reflection or transmission depends on many factors such as the DW width, Dzyaloshinskii-Moriya interaction (DMI) [25], and magnon frequency (wavelength) [9]. Recently, Kim *et al.* [26] pointed out another possible mechanism of thermally induced DW motion based on Brownian thermophoresis, which predicts a DW drifting towards the colder region in a thermal gradient.

As we have briefly described, the picture is rather complex, and the main cause of DW motion in a thermal gradient might depend on the system under investigation. Although numerical studies [19] suggest that the ET is much stronger than μSTT, a detailed comparison is still lacking. Furthermore, previous analyses focused on linear thermal gradients [19,22] where both effects are simultaneously present. However, ET and μSTT have different interaction ranges: the ET is intrinsically *local* (i.e., the DW needs to be inside the TG in order to *feel* the energy gradient and move), while the μSTT depends on the magnon propagation length [27], which can be larger than the TG extension. Therefore, the dominant effect (μSTT or ET) might depend on the distance from the TG, and the comparison between different contributions at different distances remains to be evaluated. Moreover, previous theoretical analyses were performed on perfect samples without considering the effect of pinning, which is essential for comparison with experimental observations.

In this work we study, by means of micromagnetic simulations, the DW motion induced by a *localized* Gaussian temperature profile (as would be given by a laser spot) placed at different distances from the DW in a permalloy nanostrip as sketched in Fig. 1. We separate magnonic and entropic contributions, and we reveal the main cause of DW motion at each distance. We point out the existence of a third driving force due to a thermally induced dipolar field generated by the laser spot. Such force was ignored before since most theoretical studies neglected long-range dipolar interaction [19,21,22]. Finally, by including edge roughness, we analyze the thermally induced DW motion under realistic conditions. This paper is structured as follows: Sec. II describes the numerical methods and the system under investigation. The main observations are outlined in Sec. III, while the different driving mechanisms are explained in more detail in Sec. III A (entropic torque), Sec. III B (thermally induced dipolar field), and Sec. III C (magnonic spin transfer torque). Finally, the results for a realistic strip are shown in Sec. III D, and the main conclusions are summarized in Sec. IV.

*Corresponding author: simone.moretti@usal.es

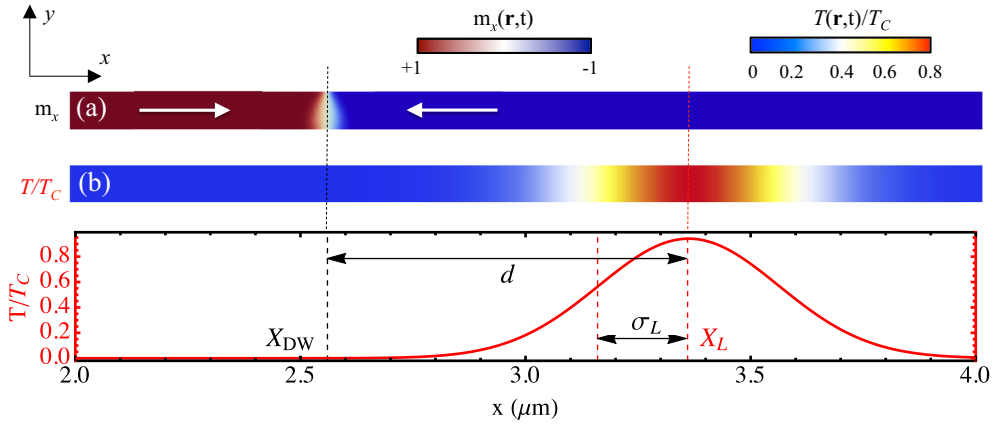

FIG. 1. (a) Initial magnetization state. (b) Temperature profile along the strip T/T_C, with reference to the laser position X_L, the distance d from the DW, and the laser width σ_L.

II. METHODS

Magnetization dynamics is analyzed in a permalloy (Py) nanostrip of length $L_x = 5.12\,\mu$m and cross section $S = (80\times10)\,\text{nm}^2$ with a head-to-head transverse DW (TW) placed and relaxed in its center ($X_{DW} = 2.56\,\mu$m). The initial magnetic configuration and reference frame are shown in Fig. 1(a). Magnetization lies in plane along the x direction, and the TW is stable for these dimensions. Magnetic evolution is studied by means of the stochastic Landau-Lifshitz-Bloch (LLB) equation [28–32]:

$$\frac{d\boldsymbol{m}}{dt} = -\gamma_0(\boldsymbol{m}\times\boldsymbol{H}_{\text{eff}}) + \frac{\gamma_0\alpha_\parallel}{m^2}(\boldsymbol{m}\cdot\boldsymbol{H}_{\text{eff}})\boldsymbol{m} - \frac{\gamma_0\alpha_\perp}{m^2}[\boldsymbol{m}\times(\boldsymbol{m}\times\boldsymbol{H}_{\text{eff}}+\boldsymbol{\eta}_\perp)] + \boldsymbol{\eta}_\parallel\,, \qquad (1)$$

where γ_0 is the gyromagnetic ratio. $\alpha_\perp = \alpha_0[1 - T/(3T_C)]$ and $\alpha_\parallel = \alpha_0(2T/3T_C)$ are the transverse and longitudinal damping parameters, respectively, where α_0 is a microscopic damping parameter coupling the spins to the lattice and T_C indicates the Curie temperature. $\boldsymbol{m}$ represents the normalized magnetization vector ($\boldsymbol{m} = \boldsymbol{M}/M_0$, with M_0 being the saturation magnetization at zero temperature), and $\boldsymbol{H}_{\text{eff}}$ is the effective magnetic field given by

$$\boldsymbol{H}_{\text{eff}} = \frac{2A(T)}{\mu_0 M_0 m_e^2}\nabla^2\boldsymbol{m} + \boldsymbol{H}_{\text{dmg}} + \frac{1}{2\tilde{\chi}_\parallel}\left(1 - \frac{m^2}{m_e^2}\right)\boldsymbol{m}. \qquad (2)$$

The first term on the right-hand side (RHS) is the exchange field [19,22] [$A(T)$ is the temperature-dependent exchange stiffness, μ_0 is the vacuum permeability, and m_e is the equilibrium magnetization module]. $\boldsymbol{H}_{\text{dmg}}$ is the demagnetizing field, while the last term represents the longitudinal exchange field, which drives the module of $\boldsymbol{m}$ towards its equilibrium value at each temperature, $m_e(T)$. $\tilde{\chi}_\parallel$ is the longitudinal susceptibility defined as $\tilde{\chi}_\parallel = (\partial m_e/\partial H_a)_{H_a\to0}$, with H_a being the external field. The choice of LLB is preferred over the conventional Landau-Lifshitz-Gilbert (LLG) equation since it allows us to describe magnetization dynamics for temperatures even close to T_C. Furthermore, it naturally includes the ET within the temperature dependence of the micromagnetic parameters $\boldsymbol{m}(T)$ and $A(T)$ [19]. In fact, in the LLB, $\boldsymbol{m}$ is not restricted to unity, and its value depends on the temperature, as well as the values of $\tilde{\chi}_\parallel$, $\alpha_\perp$, and $\alpha_\parallel$. However, the ET depends only on $\boldsymbol{m}(T)$ and $A(T)$ since they directly affect the DW energy, while the other parameters ($\tilde{\chi}_\parallel$, $\alpha_\perp$, $\alpha_\parallel$) affect the dynamics.

The function $m_e(T)$ needs to be introduced as an input into the model, and within the mean-field approximation (MFA) and in the classic limit, it is given by the Langevin function [33,34]: $m_e = \coth(x) - 1/x$, with $x = \mu_0\mu_{\text{Py}}H_a/(k_BT) + 3T_Cm_e/T$, where μ_{Py} is the Py magnetic moment and k_B is the Boltzmann constant. The second term represents the Weiss molecular field expressed in terms of T_C. For the calculation we considered $H_a \to 0$ since there is no applied field. The obtained m_e and $\tilde{\chi}_\parallel$ are shown in Fig. 2. Within the MFA the temperature dependence of the exchange stiffness is given by $A(T) = A_0m_e(T)^2$ [14,32,34], where A_0 is the exchange stiffness at $T = 0$. The dynamics of the magnetization module (the *longitudinal* dynamics) is described by the second term on the RHS of Eq. (1), proportional to $\alpha_\parallel$, and it is governed by the longitudinal exchange field in Eq. (2), proportional to $\tilde{\chi}_\parallel$. Such dynamics becomes important at $T \approx T_C$ when longitudinal and transverse relaxation times are comparable.

$\boldsymbol{\eta}_\perp$ and $\boldsymbol{\eta}_\parallel$ are transverse and longitudinal stochastic fields, which introduce thermal fluctuations, and therefore excite

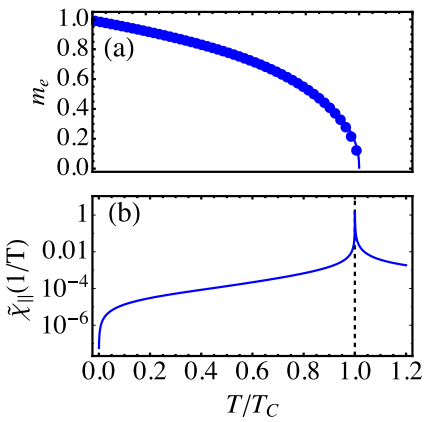

FIG. 2. (a) Equilibrium magnetization $m_e(T)$ obtained with the Langevin function [33]. Dots correspond to numerical results, while the solid line is a fit of the numerical solution. (b) Longitudinal susceptibility $\tilde{\chi}_\parallel = (\partial m_e/\partial H_a)_{H_a\to0}$.

thermal magnons, into the system. They have white-noise properties with correlators given by [31]

$$\langle \eta_{\perp}^{i}(\mathbf{0},0)\eta_{\perp}^{j}(\boldsymbol{r},t)\rangle = \frac{2k_B T(\alpha_{\perp}-\alpha_{\parallel})}{\gamma_0\mu_0 M_s^0 V\alpha_{\perp}^2}\delta_{ij}\delta(\boldsymbol{r})\delta(t),$$
$$\langle \eta_{\parallel}^{i}(\mathbf{0},0)\eta_{\parallel}^{j}(\boldsymbol{r},t)\rangle = \frac{2\gamma_0 k_B T\alpha_{\parallel}}{\mu_0 M_s^0 V}\delta_{ij}\delta(\boldsymbol{r})\delta(t), \quad (3)$$

which are obtained by imposing the Maxwell-Boltzmann distribution as the solution of the Fokker-Plank equation calculated from the stochastic LLB [31]. Note that a cutoff on the magnon wavelength is imposed by discretizing the sample in cubic cells (as commonly done in finite-difference solvers); that is, magnons with wavelength smaller than $2\Delta x$ cannot be included in the thermal noise, where Δx is the cell size. Within the LLB formalism, their contribution is still included in the temperature dependence of the micromagnetic parameters $m_e(T)$ and $A(T)$, but any flux of such small-wavelength magnons, from one cell to another, is neglected. This means that our analysis of the magnonic STT is restricted to thermal magnons with $\lambda > 2\Delta x$. For this reason we chose cells of dimensions $2.5\times5\times10$ nm in order to include a higher flux of magnons along the x direction. In Sec. III C we will see that these magnons have a very small propagation length [$L_p \sim 80$ nm, see Eq. (15)], and therefore, they can be ignored when they are excited far from the DW position since they do not reach it. Inside the TG, where they could reach the DW, their contribution is ignored, and this constitutes a limitation of our model. At the end of Sec. III C we will briefly discuss the possible effects of such small-wavelength magnons.

In summary, the ET is naturally included in the model by the temperature dependence of $\boldsymbol{m}(T)$ and $A(T)$, while magnons are excited by the stochastic fields. At a given temperature we will have both effects simultaneously. To isolate the effect of the ET we simply perform simulations without thermal field, and we label this kind of simulation as *entropic*. To isolate the effect of magnons we perform simulations by keeping $\boldsymbol{m}(T)$ and $A(T)$ constant at their $T = 0$ values, and we label this kind of simulation as *magnonic*. Simulations with the full stochastic LLB [Eq. (1)] are labeled as *full*. The magnonic simulations correspond to what one would observe within the LLG framework for $T \ll T_C$, assuming that $m_e(T)$ and $A(T)$ do not change with temperature. Indeed, we checked that for $T_L = 200{,}400$ K (where the LLG framework can be applied) the magnonic results correspond to the results of the conventional LLG.

Equation (1) is solved by the finite-difference method with customized software [23,32]. We use the mentioned cell size ($2.5\times5\times10$ nm) and a time step of 0.1 ps, testing that smaller time steps produce equal results. Typical Py parameters are considered: $A_0 = 1.3\times10^{-11}$ J/m, $M_0 = 8.6\times10^5$ A/m, $\alpha_0 = 0.02$, and $T_C = 850$ K.

The strip temperature is given by a Gaussian profile:

$$T(x) = T_0 + T_L \exp\left[-\frac{(x-X_L)^2}{2\sigma_L^2}\right], \quad (4)$$

where $T_0 = 0$ and T_L is the laser temperature. X_L is the laser spot position, and σ_L is the Gaussian profile width. For our study we chose $\sigma_L = 200$ nm, which corresponds to a laser waist of $\sqrt{2}\sigma_L \approx 280$ nm, reasonable for typical lasers [12]. We performed simulations placing the laser spot at different distances from the DW ($d = X_L - X_{DW}$). Distances correspond to integer multiples of σ_L, i.e., $d = X_L - X_{DW} = N\sigma_L$, with $N = 1,2,\ldots,10$. Simulations are performed for four different laser temperatures, $T_L = 200{,}400{,}600$, and 800 K. The temperature profile is plotted in Fig. 1(b) for $T_L = 800$ K. Five different stochastic realizations are considered when thermal fluctuations are taken into account (magnonic and full simulations). The gradient extension from X_L is approximatively equal to $3\sigma_L$; in other words, $\nabla T(X_{\mathrm{DW}}) \approx 0$ if $d > 3\sigma_L$. In fact, $\nabla T(3\sigma_L) \approx 0.1$ K/nm, and the estimated entropic field (see Sec. III A) is $\mu_0 H_E \approx 0.06$ mT. Furthermore, $T = 0$ K is imposed for $d > 4.5\sigma_L$, so that $\nabla T(X_{\mathrm{DW}}) = \mu_0 H_E = 0$ if $d > 4.5\sigma_L$. We simulate an infinite strip by removing the magnetic charges appearing on both sides of the computational region [35]. The simulation time window is varied depending on d and the DW velocity, with a maximum simulation time of $t_{\max} = 500$ ns.

III. RESULTS AND DISCUSSION

Figure 3 shows the normalized DW displacement $\Delta x/d$ as a function of time for the entropic, magnonic, and full cases, calculated with $T_L = 800$ K, for three different distances, as labeled on the top of each column: $d = 2\sigma_L$ [Figs. 3(a)–3(c)], $d = 4\sigma_L$ [Figs. 3(d)–3(f)], and $d = 6\sigma_L$ [Figs. 3(g)–3(i)]. The displacement is normalized to the laser distance d, and therefore, $\Delta x/d = 1$ indicates that the DW has reached the laser spot.

For $d = 2\sigma_L$ the DW moves towards the laser spot for both the magnonic [Fig. 3(b)] and entropic [Fig. 3(a)] cases [and therefore obviously in the full case; Fig. 3(c)]. The DW is inside the TG [$\nabla T(X_{\mathrm{DW}}) \neq 0$], and its motion can be attributed mostly to the ET [19–21]. In the magnonic case the motion could be given by a magnon stream passing adiabatically through the DW and also by the effect of an averaged ET. Note that thermal magnons, apart from the μSTT, also introduce an averaged ET [21,23]: where the temperature is higher, the *averaged* M_s (over more cells) is lower (as in the entropic case) due to higher thermal fluctuation. More precisely, we recall that also the temperature dependence of $\boldsymbol{m}$ and A is given by averaged high-frequency magnons which cannot be included in the thermal fluctuations due to the spatial discretization. This averaged ET is, however, a small contribution compared to the one given by high-frequency magnons, as can be seen by the time scale in Figs. 3(a) and 3(b).

For $d = 4\sigma_L$ the DW moves towards the hotter region in the entropic case [Fig. 3(d)] and towards the colder region in the magnonic case [Fig. 3(e)]. The latter could be attributed to μSTT (Sec. III C), while the first effect is unexpected since at $d = 4\sigma_L$, $\nabla T(X_{\mathrm{DW}}) \approx 0$ and the ET should have no effect (we recall that the gradient extension is approximatively $3\sigma_L$). This is even more visible in the $d = 6\sigma_L$ case where, although it is certain that $\nabla T(X_{\mathrm{DW}}) = 0$, the DW moves towards the hotter region [Fig. 3(g)]. Note that the DW moves with different velocities when it is outside ($x > X_L - 3\sigma_L$) or inside ($x < X_L - 3\sigma_L$) the TG. We conclude that there must be another long-range driving force, not related to magnons, that drives the DW in this case. As we will discuss in Sec. III B,

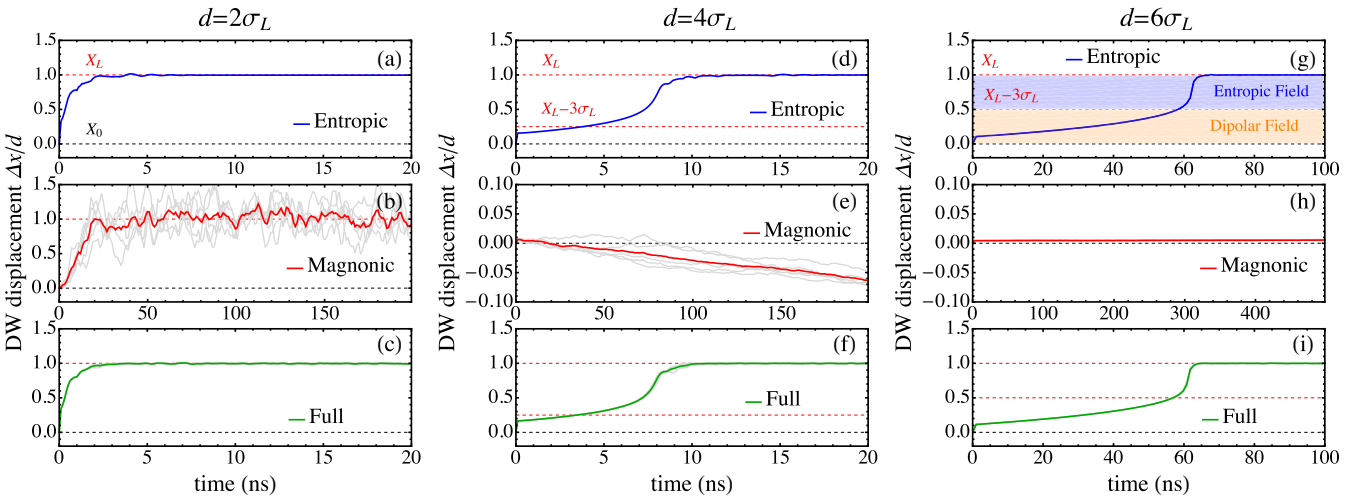

FIG. 3. DW displacement as a function of time for (a)–(c) $d = 2\sigma_L$, (d)–(f) $d = 4\sigma_L$, and (g)–(i) $d = 6\sigma_L$ for the entropic, magnonic, and full cases as labeled in each plot. Displacement Δx is normalized to d: a displacement of 1 means that the DW has reached the center of the laser spot. X_L indicates the laser position, X_0 is the DW position, and $X_L - 3\sigma_L$ is the extension of the TG, i.e., the region where $\nabla T(x) \neq 0$.

this force is given by a thermally induced dipolar field. In the magnonic case [Fig. 3(h)] the DW does not move, compatible with μSTT if we assume that magnons are already damped for such a distance ($d = 6\sigma_L = 1.2\ \mu$m). Indeed, we estimated a magnon propagation length of 330 nm ($\ll 1.2\,\mu$m) for our sample (Sec. III C). Different laser temperatures ($T_L =$ 200,400,600 K) produce qualitatively similar behaviors for all the distances. Furthermore, for all cases the full simulations are very similar to the entropic simulations, suggesting that the ET dominates over the μSTT [36].

Figure 4(a) shows the averaged DW velocity [37] as a function of laser distance. As mentioned, the ET dominates the DW dynamics, and in fact, entropic and full velocities almost coincide. The averaged velocity decreases with distance, but it is different from zero even for the maximum distance we analyzed ($d = 10\sigma_L = 2\,\mu$m), meaning that, with enough time $t > t_{\max}$, the DW would reach the laser spot since the velocities are always positive (towards the hot part). On the other hand, magnonic simulations give rise to positive velocity for $d = 2,3\sigma_L$ due to an averaged ET, negative velocities (towards the cold part) for $d = 4,5\sigma_L$, and almost null velocities for $d \geqslant 6\sigma_L$. In all the cases, the velocities due to μSTT are much smaller than the entropic velocities, in agreement with previous predictions [19]. The details of the averaged magnon velocities are shown in the inset of Fig. 4(a).

Figure 4(b) displays the average full velocity as a function of laser distance for four different laser temperatures: at $d = 2,3\sigma_L$ the maximum DW velocity is observed for $T_L = 400$ K due to the Walker breakdown (WB) threshold at $T_L = 600$ K, predicted also for thermally induced DW motion [19]: Below 600 K the entropic field (Sec. III A) is compensated by the DW shape anisotropy, and the DW moves rigidly without changing its internal structure. For $T_L > 600$ K the DW anisotropy cannot compensate the entropic field, and the DW precesses, changing its internal structure and resulting in a slower velocity, as can be seen in a movie in the Supplemental Material [38]. On the other hand, for $d \geqslant 4\sigma_L$ the maximum temperature coincides with maximum velocity since the thermally induced dipolar field is below the WB and the DW moves faster while outside the TG. In what follows we analyze each contribution separately.

A. Entropic field

The ET originates from the fact the DW free energy $\Delta F(T)$ decreases with temperature and, as a consequence, the DW

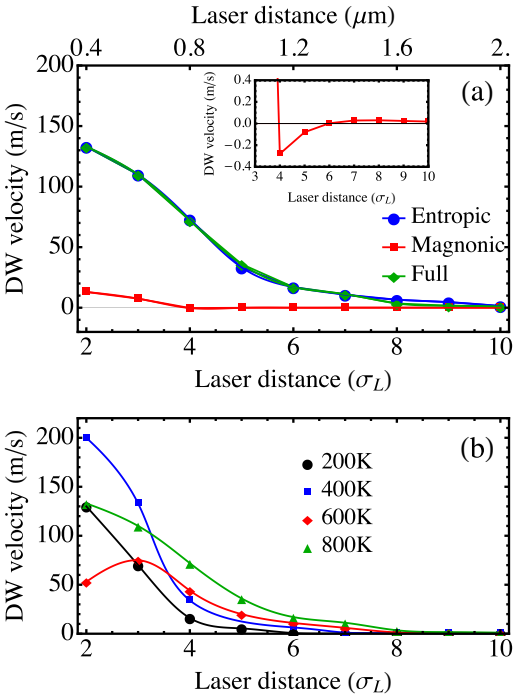

FIG. 4. (a) DW average velocity as a function of laser distance for the entropic (blue dots), magnonic (red squares), and full (green diamonds) cases. The inset shows a detail of the magnonic case from $d = 4\sigma_L$ to show the negative small velocities, which are not visible in comparison with the entropic velocities. (b) DW average full velocities for different temperatures. At $d = 2\sigma_L$ the maximum velocity is observed at $T = 400$ K due to the WB threshold at $T \geqslant 600$ K.

moves towards the hotter region in order to minimize its free energy [19,20,22]. It is called entropic since DW entropy increases with temperature and leads to the overall decrease of the free energy [19,20,39], $\Delta F = \Delta U - T\Delta S$, with ΔU being the DW internal energy [19,39] and ΔS being the DW entropy [19,39]. In the thermodynamic picture of LLB, entropy is included in the temperature-dependent DW free-energy density [19,39,40],

$$\epsilon_{\mathrm{DW}}(T) = 4\sqrt{A(T)[K_0(T) + K_S(T)\sin^2\phi]}, \tag{5}$$

where $K_0(T)$ and K_S are effective anisotropy constants and ϕ is the internal DW angle. In the case of permalloy, the anisotropies are both of magnetostatic origin (shape anisotropies), and they are given by

$$\begin{aligned} K_0(T) &= \tfrac{1}{2}\mu_0 M_0^2 (N_y - N_x) m(T)^2, \\ K_S(T) &= \tfrac{1}{2}\mu_0 M_0^2 (N_z - N_y) m(T)^2, \end{aligned} \tag{6}$$

where $N_{x,y,z}$ are the demagnetizing factors. As in MFA, also, $A(T)$ decreases with T as $m(T)^2$, and $\epsilon_{\mathrm{DW}}(T)$ decreases as

$$\epsilon_{\mathrm{DW}}(T) = 4\sqrt{A_0\left(K_0^0 + K_S^0 \sin^2\phi\right)} m(T)^2, \tag{7}$$

where K_0^0 and K_S^0 are the shape anisotropies at $T = 0$. Therefore, the temperature gradient introduces a DW energy gradient, which leads to the equivalent field (the so-called entropic field)

$$\begin{aligned} \mu_0 \boldsymbol{H}_E &= -\frac{1}{2m_e M_0}\nabla\epsilon_{\mathrm{DW}} = -\frac{1}{2m_e M_0}\frac{\partial\epsilon_{\mathrm{DW}}}{\partial T}\frac{\partial T}{\partial x}\hat{x} \\ &= -\frac{4A_0}{M_0\Delta_0}\frac{\partial m}{\partial T}\frac{\partial T}{\partial x}\hat{x}, \end{aligned} \tag{8}$$

where the gradient is only along $\hat{x}$ and

$$\frac{\partial\epsilon_{\mathrm{DW}}(T)}{\partial T} = 2m\epsilon_{\mathrm{DW}}^0\frac{\partial m}{\partial T} = \frac{8mA_0}{\Delta_0}\frac{\partial m}{\partial T}. \tag{9}$$

$\Delta_0 = \sqrt{A_0/(K_0 + K_S^0\sin^2\phi)}$ and ϵ_{DW}^0 are the DW width and energy at $T = 0$, respectively.

In Ref. [19] Schlickeiser *et al.* proposed an analytical expression for $\mu_0 H_E^*$ by solving the LLB equation in the one-dimensional (1D) approximation. Within the MFA their expression is indeed equivalent to Eq. (8). In fact,

$$\begin{aligned} \mu_0 \boldsymbol{H}_E^* &= -\frac{2}{\Delta(T)M_0}\frac{\partial A(T)}{\partial T}\frac{\partial T}{\partial x}\hat{x} \\ &\overset{\mathrm{MFA}}{=} -\frac{4A_0}{\Delta_0 M_s}\frac{\partial m}{\partial T}\frac{\partial T}{\partial x}\hat{x}. \end{aligned} \tag{10}$$

Figure 5(a) shows the strip temperature profile for $T_L = 800\,\mathrm{K}$ and $X_L = 3.16\,\mu\mathrm{m}$. Figure 5(b) depicts the corresponding DW energy profile $\epsilon_{\mathrm{DW}}(T(x))$ [Eq. (7)], and Fig. 5(c) shows the resulting entropic field $\mu_0 H_E(x)$ [Eq. (8)]. The entropic field always pushes the DW towards the center of the laser spot where $\mu_0 H_E = 0$ since $\nabla T = 0$. Note that, indeed, the ET is *local* because it depends on $\nabla T(x)$: If $\nabla T(x) = 0$, then $\mu_0 H_E(x) = 0$. The maximum field is approximatively at $d = 1\sigma_L$, where ∇T is maximum.

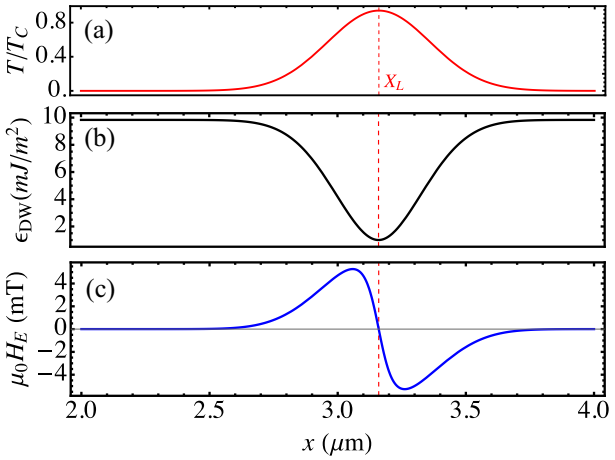

FIG. 5. (a) Temperature profile $T(x)$ for $X_L = 3.16\,\mu\mathrm{m}$ and $T_L = 800\,\mathrm{K}$. (b) Corresponding DW energy profile $\epsilon_{DW}(T(x))$ as given by Eq. (7) and (c) the resulting entropic field as predicted by Eq. (8).

B. Thermally induced dipolar field

Since in the entropic simulations the DW moves even when $\nabla T(X_{\mathrm{DW}}) = 0$, there must be another force responsible for its motion at large distances. A natural candidate is the demagnetizing field, which is a long-range interaction. Indeed, a thermally induced dipolar field (TIDF) was found to be the responsible for the DW motion at large distances. Figure 6(a) displays the TIDF H_{dip} of a uniform magnetized strip with the laser spot. Strip magnetization is saturated along x ($m_x = -1$), and the TIDF is calculated by subtracting the demagnetizing field of the strip without the laser spot from the demagnetizing field of the same uniform strip with the laser spot (in this way we can isolate the effect of the laser). The field has a minimum at X_L and positive tails outside the thermal gradient [Figs. 6(a) and 6(c)]. The laser temperature is set to the minimum value $T_L = 200\,\mathrm{K}$. The TIDF is due to the volume charges $\rho_M = -\nabla\cdot\mathbf{M}$, shown in Fig. 6(b), which arise from the variation of the magnetization module. Positive and negative charges, on the left and right sides of X_L, respectively, combine their effects in the center, giving rise to the minimum value of the TIDF (maximum in module), while they compete with each other outside the laser spot, giving rise to the decaying behavior.

A comparison between the TIDF and the entropic field is shown in Fig. 6(c). As expected, beyond $2\sigma_L$ the TIDF is much larger than the entropic field, which rapidly decays to zero outside the TG. $\mu_0 H_E$ decays as $\nabla T \propto (x - X_L)e^{-|x-x_L|^2/(2\sigma_L^2)}$, as expected, while the TIDF decays as $1/x^3$, as expected for a dipolar field [Fig. 6(c)]. Before $2\sigma_L$ the comparison has no meaning since the TIDF is calculated for a uniform magnetization and it would change once the DW approaches the laser center.

To further check our explanation, a 1D model was implemented following Ref. [19]. The model originally includes the ET, while the TIDF is added by fitting the micromagnetic TIDF [Fig. 6(a)]. The field is set different from zero only if $d > 2\sigma_L$ since it has no meaning for closer distances, as previously mentioned. The 1D model equations governing the

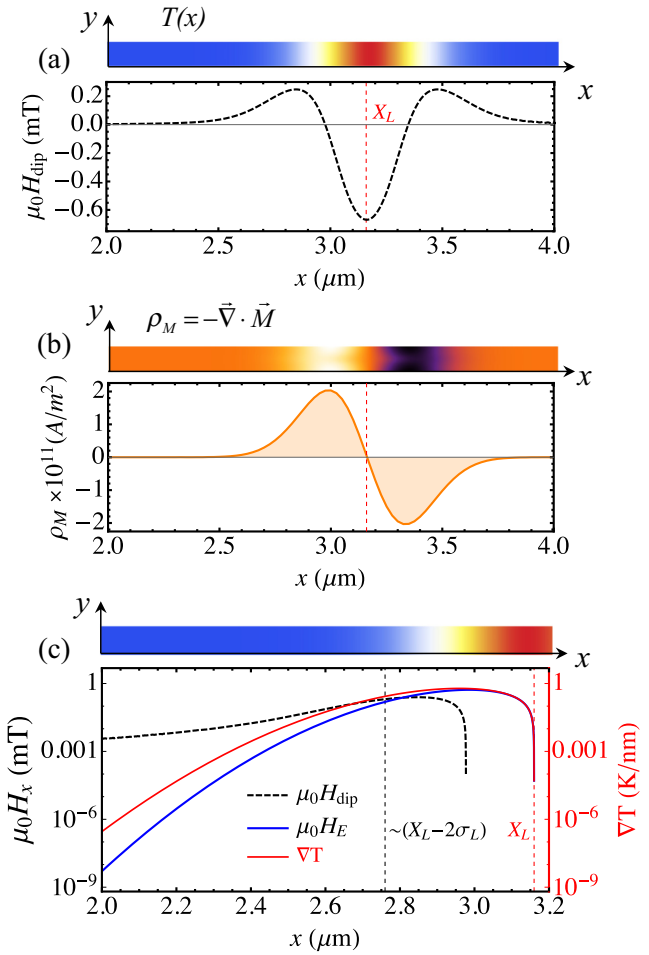

FIG. 6. (a) Thermally induced dipolar field and (b) volume charges $\rho_M = -\nabla \cdot \mathbf{M}$ for $X_L = 3.16\,\mu$m and $T_L = 200$ K. (c) Comparison between the entropic and demagnetizing field. Beyond $2\sigma_L$ from the laser spot, the demagnetizing field dominates.

DW internal angle ϕ and DW position q read

$$\dot{\phi} = \gamma_0\left[\left(H_{\rm dip} - \frac{4A_0}{\mu_0 M_0 \Delta_0}\frac{\partial m}{\partial x}\right) - \alpha_\perp \frac{K_S^0}{\mu_0 M_0}\sin(2\phi)\right],$$
$$m\frac{\dot{q}}{\Delta_0} = \gamma_0\left[\alpha_\perp\left(H_{\rm dip} + \frac{4A_0}{\mu_0 M_0 \Delta_0}\frac{\partial m}{\partial x}\right) + \frac{K_S^0}{\mu_0 M_0}\sin(2\phi)\right]. \quad (11)$$

The second term on the RHS of Eq. (11) is the entropic field as derived in Eq. (8), while the first term is the TIDF. Both fields depend on the DW position q. The results of the 1D model calculations are plotted in Fig. 7. For $d = 2\sigma_L$ [Fig. 7(a)] the model gives equal results with and without TIDF, as expected (the TIDF is null in this case), and the agreement with simulations is good. For $d = 4\sigma_L$ the model without TIDF (purple dashed line) predicts no DW motion, as expected from the ET since the DW is outside the temperature gradient. On the other hand, the model with the TIDF (black dotted line) predicts DW motion and shows better agreement with simulations, confirming our hypothesis.

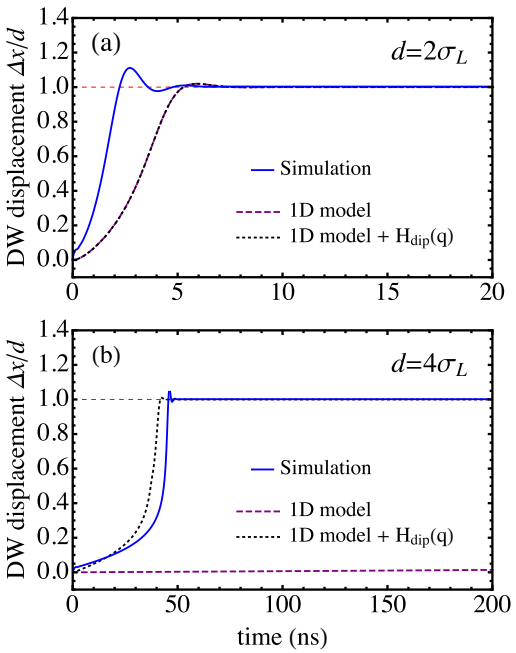

FIG. 7. DW displacement as a function of time as predicted by the 1D model with or without the demagnetizing field for (a) $d = 2\sigma_L$ and (b) $d = 4\sigma_L$. The model without a demagnetizing field does not predict any motion for $d \geqslant 4\sigma_L$.

By using the 1D model it is also possible to estimate the WB thermal gradient:

$$\nabla T_W = \frac{\Delta_0 \alpha_\perp K_S^0}{4A_0(\partial m/\partial T)}. \quad (12)$$

Due to the presence of $\partial m/\partial T$ the WB also depends on the absolute temperature T, which affects $\partial m/\partial T$ [19]. The WB as function of temperature is plotted in Fig. 8. The blue points represent the maximum value of $\nabla T(x)$ (being a Gaussian profile, ∇T is not constant) applied in the simulations for different laser temperatures. The crossing of the WB occurs at $T \approx 660$ K, in reasonable agreement with our observation [$T = 600$ K, Fig. 4(b)]. The small difference could be given

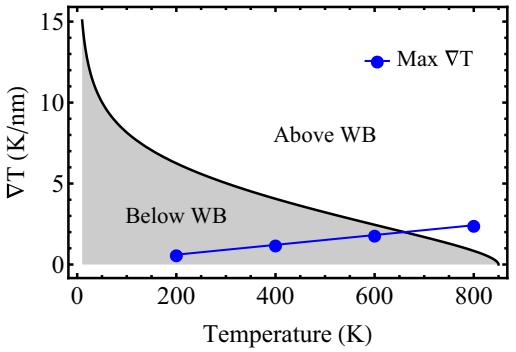

FIG. 8. WB thermal gradient as a function of temperature [Eq. (12)]. For a Gaussian profile, such as the one applied in our simulations, ∇T is not constant; the blue points represent the maximum value of ∇T for each temperature, which occurs approximatively at $1\sigma_L$ from the laser spot center.

by the effect of the TIDF or by the uncertainty on the 1D parameters (K_S^0, Δ_0) [41].

Magnetostatic effects on thermally induced DW motion were already discussed by Berger [42]. Despite the common magnetostatic origin, the TIDF shown here presents some differences: In Ref. [42] the thermal gradient affects the magnetostatic energy of the domains (much more relevant in bulk samples such as the ones analyzed by Berger), whereas, here, it is the Gaussian temperature profile by itself that generates new magnetostatic volume charges which give rise to the TIDF.

C. Magnonic spin transfer torque

Magnons can drive the DW towards either the hot or the cold part depending on their interaction with the DW: they drive the DW towards the cold part if they are reflected by the DW [8,9,24] due to linear momentum transfer, while they drive the DW towards the hot part if they pass through the DW due to angular momentum transfer [9,10,21]. As already mentioned, we observe DW motion towards the hot part for $d = 2,3\sigma_L$ [Fig. 3(b)], DW motion towards the cold part for $d = 4,5\sigma_L$ [Fig. 3(e), inset of Fig. 4(a)], and no DW motion for $d \geqslant 6\sigma_L$ [Fig. 3(h), inset of Fig. 4(a)].

At $d = 2,3\sigma_L$ the motion is probably due to an averaged ET (as noted in Sec. III), and it is not possible to isolate the effect of magnons. For $d \geqslant 6\sigma_L$ the magnons are already damped, and therefore, they do not interact with the DW. In fact, by fitting the magnon accumulation [27] $\delta m_y(x,t) = m_y(x,t) - m_y(x,0)$, we estimate a magnon propagation length $L_p = 330$ nm [Fig. 9(a)]. This means that at $d = 4,5\sigma_L$ (200 and 400 nm, respectively, from the end of the laser spot) the DW is within the magnon propagation length, while at $d = 6\sigma_L$ the DW is at $\approx 2L_p$, where magnons are clearly damped. Therefore, at $d = 4,5\sigma_L$, where $\nabla T(X_{DW}) \approx 0$, the motion towards the cold part should be given by the μSTT. To better understand such behavior, thermally excited magnons were analyzed by means of two-dimensional fast Fourier transform (FFT) in the middle of the strip ($y_0 = 40$ nm), i.e., by calculating the FFT power [8]

$$\tilde{m_y}(\omega,k_x) = \mathcal{F}_{2D}[m_y(x,y_0,t) - m_y(x,y_0,0)], \qquad (13)$$

where the FFT is calculated with respect to $\{x,t\}$. Figure 9(b) shows the normalized magnon frequency spectrum $\sum_{k_x} \tilde{m_y}(\omega,k_x)$ at the laser spot (LS; region 1: $X_L \pm 330$ nm) and right before the LS [region 2: $(X_L - 5\sigma_L) \pm 330$ nm]. At the LS (black dots) magnons have a wide range of frequency, while before the laser spot (green line) only low-frequency magnons have propagated, in agreement with previous observation [27]. The cutoff at $f_0 \approx 9$ GHz is due to lateral width confinement [8]. Therefore, the average magnon propagation length, previously calculated [Fig. 9(a)], is mainly related to low-frequency magnons. This is a relevant observation since the magnon frequency strongly affects magnon transmission or reflection at the DW [9]. In particular, low-frequency magnons are likely to be reflected [8,9] and would produce motion towards the cold part.

To further understand the interaction between magnons and the DW, the DW dynamics excited by monochromatic spin waves (SWs) was analyzed in the same Py strip.

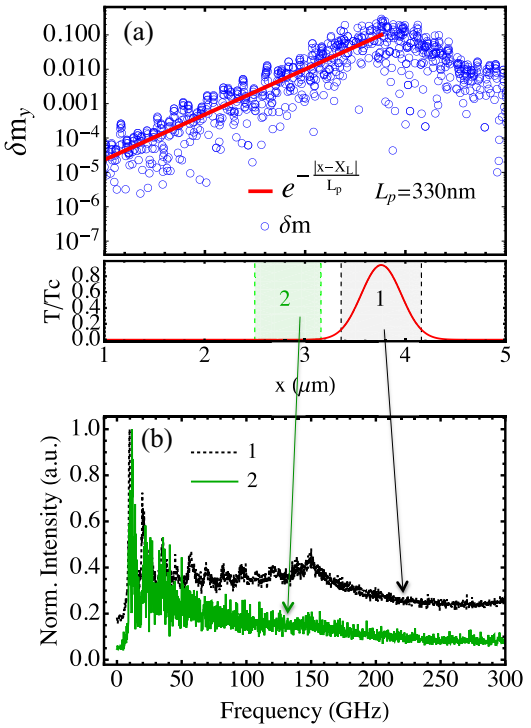

FIG. 9. (a) Magnon accumulation as defined in Ref. [27] [$\delta m_y(x,t) = m_y(x,t) - m_y(x,0)$] for $X_L = 3.76\,\mu$m. The time t at which the magnon accumulation is calculated is $t = 10$ ns, long enough that magnons have propagated along the strip and have reached an equilibrium state. Magnons decay exponentially, as shown by the fit with $e^{-|x-X_L|/L_p}$, where $L_p = 330$ nm is the magnon propagation length. (b) FFT intensity as a function of magnon frequency in region 1, $X_L \pm 330$ nm (below the laser spot, black dots), and region 2, $(X_L - 5\sigma_L) \pm 330$ nm (outside the laser spot, green line).

SWs were locally excited by a transverse sinusoidal field $\boldsymbol{H}_a(x) = H_0 \sin(2\pi f)\hat{y}$ at a distance of 100 nm from the DW [Fig. 10(a)]. The excitation region has dimensions $10\times80\times10$ nm, and $\mu_0 H_0$ is set to 10 mT. The DW dynamics by different frequencies is shown in Fig. 10(b), while the spin-wave propagation length as a function of frequency is depicted in Fig. 10(c). Consistent with previous analysis [8,11] the DW moves towards the cold part (in this case cold means away from the antenna position, i.e., in the same direction as magnon propagation) for low frequency, $f = 18,25$ GHz, while no motion towards the hot direction is observed within the maximum applied frequency, $f_{\max} = 100$ GHz [Fig. 10(b)]. Moreover, the monochromatic analysis allows us to study the frequency-dependent magnon propagation length, and indeed, it confirms that magnon propagation length decays with the magnon frequency [Fig. 10(c)]. Note that the propagation length of low-frequency magnons is in good agreement with our calculation for thermal magnons ($L_p = 330$ nm). Furthermore, following Ref. [27], the frequency-dependent propagation length $L_p(\omega)$ can be estimated as $1/(\alpha_\perp \omega)\partial\omega/\partial k$, and $\partial\omega/\partial k$ can be calculated from the spin-wave dispersion relation in our system [43],

$$\omega = \omega_0 + l_{\text{ex}}^2 \omega_M k^2, \qquad (14)$$

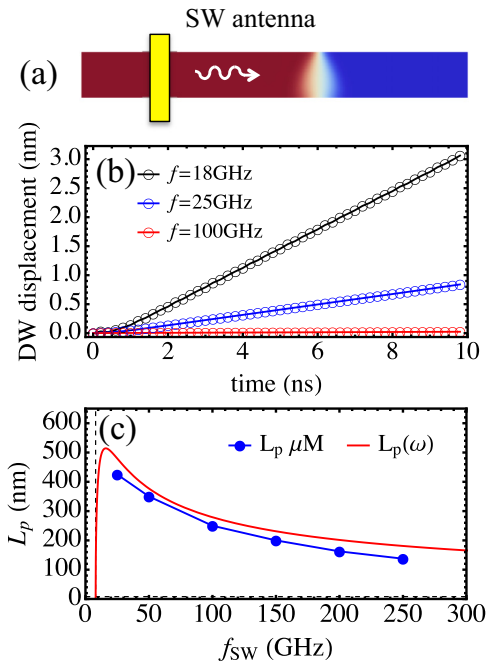

FIG. 10. (a) Schematic representation of the spin wave simulations setup. (b) DW displacement as a function of time for different frequencies. The maximum displacement is obtained for the lowest frequency ($f = 18$ GHz). (c) SW propagation length as a function of SW frequency.

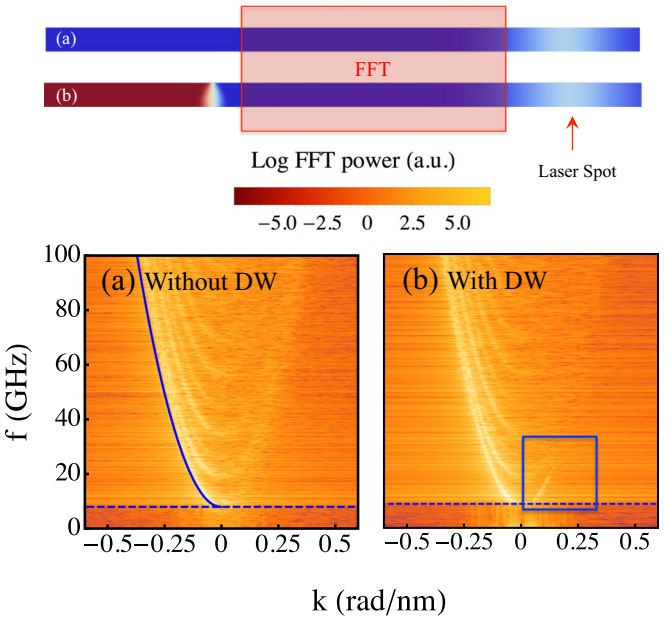

FIG. 11. Log FFT intensity as a function of frequency f and wave vector k calculated at $X_0 \pm 330$ nm (b) with and (a) without the DW. The plot shows typical SW dispersion curves. The left branches correspond to magnons propagating from right to left (away from the laser spot), while the right branches correspond to magnons propagating from left to right (towards the laser spot). A small right branch at low frequency can be observed in the case with DW in (b), which corresponds to magnons reflected by the DW. The blue dashed line indicates the cutoff at $f \approx 9$ GHz, while the blue solid line in (a) corresponds to Eq. (14), which shows good agreement with the FFT intensity.

where l_{ex} is the exchange length and $\omega_M = \gamma_0 M_0 m_e(T)$. The cutoff frequency $\omega_0 = 2\pi f_0$ is taken from simulations [this expression for the spin-wave dispersion relation will be compared with the two-dimensional FFT intensity in Fig. 11(a), giving a good agreement]. We finally obtain

$$L_p(\omega) = \frac{1}{\alpha_\perp \omega}\frac{\partial \omega}{\partial k} = \frac{2l_{ex}}{\alpha_\perp}\frac{[\omega_M(\omega-\omega_0)]^{1/2}}{\omega}. \quad (15)$$

Equation (15) is also plotted in Fig. 10, showing good agreement with the simulation results. At high frequency, where $l_{ex}^2 \omega_M k^2 \gg \omega_0$, Eq. (15) simply reduces to $L_p \cong \lambda/(\pi\alpha)$, where λ is the magnon wavelength [27].

In the laser-spot case, an additional proof of magnon reflection is given by the FFT power in the region $X_0 \pm 330$ nm, where X_0 is chosen to remain outside both the TG and the DW, as sketched in Fig. 11. The FFT is performed with [Fig. 11(b)] or without [Fig. 11(a)] the DW. The left bright branches correspond to magnons propagating from right to left, moving away from the laser spot, as expected. In the FFT with the DW [Fig. 11(b)] a small branch appears on the right side, which corresponds to magnons propagating from left to right, towards the laser spot, as a consequence of reflection by the DW [8]. Therefore, we conclude that the DW motion towards the cold part is due to low-frequency magnons, excited by the laser, which have a larger propagation length and are reflected by the DW. The result is different from that predicted by Kim and Tserkovnyak [21], where DW was supposed to move towards the hotter region due to magnon transmission through the DW. The difference is probably due to the different magnon wavelengths: in Ref. [21] the authors assumed that the thermal magnon wavelength is much shorter than the DW width, focusing on magnon transmission and the adiabatic STT. In our case, low-frequency (large-wavelength) modes dominate outside the TG due to their larger propagation length, and they are mainly reflected by the DW. From Eq. (14) we can also estimate the wavelength of the reflected magnons. The frequency range of the reflected branch in Fig. 11(b) is approximately $f_0 < f < 20$ GHz, which corresponds to a wavelength range $50 < \lambda < 400$ nm, larger than or comparable to the DW width parameter $\Delta_0 = 30$ nm. Inside the TG ($d = 2\sigma_L$) the motion is towards the hotter region, consistent with the result of Kim and Tserkovnyak [21]. In the full simulations the DW moves towards the hot part for $d = 4,5\sigma_L$, meaning that the dipolar field is stronger than the μSTT in this system. As noted in Sec. II, our analysis of the magnonic STT neglects magnons with $\lambda < 5$ nm. Due to their small propagation length ($L_p \sim 80$ nm) they can have an effect only at $d = 2,3\sigma_L$, when the DW is inside the TG. Since their wavelength is much smaller than the DW width, they are expected to pass adiabatically through the DW, moving it towards the hotter region like the ET. This would lead to higher velocities for the magnonic case at $d = 2,3\sigma_L$; however, their contribution is expected to be small since their propagation length is comparable to the full DW width ($\pi\Delta_0 \sim 90$ nm), and therefore, angular momentum transfer is strongly reduced.

D. Realistic sample

Our previous results, as well as former theoretical investigations [19,21,24], were obtained for a perfect strip where

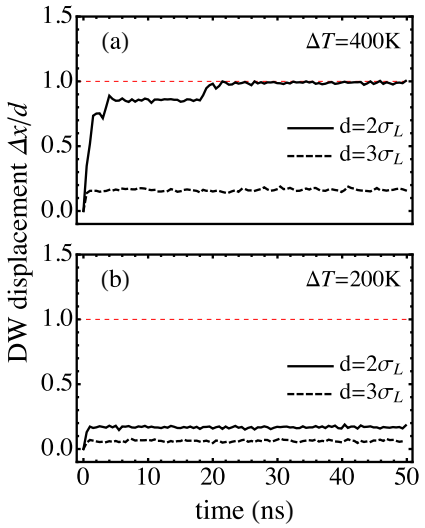

FIG. 12. DW displacement as a function of time for (a) $\Delta T = 400\,\mathrm{K}$ and (b) $\Delta T = 200\,\mathrm{K}$ for $d = 2\sigma_L$ (black solid line) and $d = 3\sigma_L$ (black dashed line). The DW reaches the laser spot (red dashed line at $\Delta x/d = 1$) only for $\Delta T = 400\,\mathrm{K}$ at $d = 2\sigma_L$.

even a small driving force was able to move the DW. However, it is well known that defects or inhomogeneities give rise to DW pinning and a finite propagation field ($H_p \neq 0$) below which the DW remains pinned. We have also analyzed DW motion by TG under realistic conditions to see in which case the TG is strong enough to depin the DW. The introduction of edge roughness with a characteristic size of 2.5 nm gives rise to a DW propagation field of $\mu_0 H_p = (3.5 \pm 0.5)\,\mathrm{mT}$. Also in this case the sample temperature follows Eq. (4), but the strip temperature T_0 is set to $T_0 = 300\,\mathrm{K}$, as it would be in conventional experiments. Considering the same ΔT as in the previous analysis and in order to remain below T_C, we can apply only $\Delta T = 400\,\mathrm{K}$ and $\Delta T = 200\,\mathrm{K}$. As shown in Fig. 12 and in the corresponding movie [41], the DW moves towards the laser spot only if it is close enough to the laser spot ($d \leqslant 2\sigma_L$) and only if $\Delta T = 400\,\mathrm{K}$. Therefore, under realistic conditions, long-range dipolar field and μSTT are not strong enough to move the DW as they are likely hindered below the propagation field in typical experiments. This observation is indeed in agreement with recent experimental observation [12] where the DW motion towards the (close) laser spot was successfully explained by the sole effect of ET [12].

IV. CONCLUSIONS

DW motion by Gaussian temperature profiles was analyzed in a Py strip under perfect and realistic conditions. Apart from the already known entropic and magnonic contributions, a third driving force was observed due to a thermally induced dipolar field. Such force drives the DW towards the hotter region. An expression for the entropic field was derived in terms of the DW energy and compared with previous expressions showing equal results. The entropic torque pushes the DW towards the hot part and dominates the DW dynamic when the DW is within the TG, while the dipolar field dominates when the DW is outside the TG. In fact, the μSTT drives the DW towards the cold part due to the prevalence of low-frequency magnons, which propagate over larger distances ($L_p \approx 330\,\mathrm{nm}$) and are reflected by the DW in the studied sample. Finally, under realistic conditions, the entropic torque is strong enough to move the DW only if the laser spot is closer than $2\sigma_L$ and $\Delta T \geqslant 400\,\mathrm{K}$. These conclusions can be generalized to other in-plane samples, but we cannot rule out that, in a system with low damping the magnonic STT could overcome the thermally induced dipolar field outside the TG. These results give important insights into the different mechanisms responsible for DW motion under thermal gradients and allows for comparison with experimental results in these systems.

ACKNOWLEDGMENTS

S.M. would like to thank M. Voto and R. Yanes-Diaz for useful discussions. This work was supported by Project WALL, FP7- PEOPLE-2013-ITN 608031 from the European Commission, Project No. MAT2014-52477-C5-4-P from the Spanish government, and Projects No. SA282U14 and No. SA090U16 from the Junta de Castilla y Leon.

[1] D. Allwood, Science **309**, 1688 (2005).
[2] S. S. P. Parkin, M. Hayashi, and L. Thomas, Science **320**, 190 (2008).
[3] N. L. Schryer and L. R. Walker, J. Appl. Phys. **45**, 5406 (1974).
[4] J. Slonczewski, J. Magn. Magn. Mater. **159**, L1 (1996).
[5] L. Berger, J. Appl. Phys. **55**, 1954 (1984).
[6] I. M. Miron, T. Moore, H. Szambolics, L. D. Buda-Prejbeanu, S. Auffret, B. Rodmacq, S. Pizzini, J. Vogel, M. Bonfim, A. Schuhl, and G. Gaudin, Nat. Mater. **10**, 419 (2011).
[7] S. Emori, U. Bauer, S.-M. Ahn, E. Martinez, and G. S. D. Beach, Nat. Mater. **12**, 611 (2013).
[8] D.-s. Han, S.-k. Kim, J.-y. Lee, S. J. Hermsdoerfer, H. Schultheiss, B. Leven, and B. Hillebrands, Appl. Phys. Lett. **94**, 112502 (2009).
[9] X.-g. Wang, G.-h. Guo, Y.-z. Nie, G.-f. Zhang, and Z.-x. Li, Phys. Rev. B **86**, 054445 (2012).
[10] P. Yan, X. S. Wang, and X. R. Wang, Phys. Rev. Lett. **107**, 177207 (2011).
[11] J.-S. Kim, M. Stärk, M. Kläui, J. Yoon, C.-Y. You, L. Lopez-Diaz, and E. Martinez, Phys. Rev. B **85**, 174428 (2012).
[12] J.-P. Tetienne, T. Hingant, J.-V. Kim, L. H. Diez, J.-P. Adam, K. Garcia, J.-F. Roch, S. Rohart, A. Thiaville, D. Ravelosona, and V. Jacques, Science **344**, 1366 (2014).
[13] J. Torrejon, G. Malinowski, M. Pelloux, R. Weil, A. Thiaville, J. Curiale, D. Lacour, F. Montaigne, and M. Hehn, Phys. Rev. Lett. **109**, 106601 (2012).
[14] A. J. Ramsay, P. E. Roy, J. A. Haigh, R. M. Otxoa, A. C. Irvine, T. Janda, R. P. Campion, B. L. Gallagher, and J. Wunderlich, Phys. Rev. Lett. **114**, 067202 (2015).
[15] W. Jiang, P. Upadhyaya, Y. Fan, J. Zhao, M. Wang, L.-T. Chang, M. Lang, K. L. Wong, M. Lewis, Y.-T. Lin, J. Tang, S. Cherepov,

X. Zhou, Y. Tserkovnyak, R. N. Schwartz, and K. L. Wang, Phys. Rev. Lett. **110**, 177202 (2013).
[16] G. E. W. Bauer, E. Saitoh, and B. J. van Wees, Nat. Mater. **11**, 391 (2012).
[17] S. Selzer, U. Atxitia, U. Ritzmann, D. Hinzke, and U. Nowak, Phys. Rev. Lett. **117**, 107201 (2016).
[18] C. Safranski, I. Barsukov, H. K. Lee, T. Schneider, A. Jara, A. Smith, H. Chang, K. Lenz, J. Lindner, Y. Tserkovnyak, M. Wu, and I. Krivorotov, arXiv:1611.00887.
[19] F. Schlickeiser, U. Ritzmann, D. Hinzke, and U. Nowak, Phys. Rev. Lett. **113**, 097201 (2014).
[20] X. S. Wang and X. R. Wang, Phys. Rev. B **90**, 014414 (2014).
[21] S. K. Kim and Y. Tserkovnyak, Phys. Rev. B **92**, 020410(R) (2015).
[22] D. Hinzke and U. Nowak, Phys. Rev. Lett. **107**, 027205 (2011).
[23] V. Raposo, S. Moretti, M. A. Hernandez, and E. Martinez, Appl. Phys. Lett. **108**, 042405 (2016).
[24] P. Yan, Y. Cao, and J. Sinova, Phys. Rev. B **92**, 100408 (2015).
[25] W. Wang, M. Albert, M. Beg, M.-A. Bisotti, D. Chernyshenko, D. Cortés-Ortuño, I. Hawke, and H. Fangohr, Phys. Rev. Lett. **114**, 087203 (2015).
[26] S. K. Kim, O. Tchernyshyov, and Y. Tserkovnyak, Phys. Rev. B **92**, 020402 (2015).
[27] U. Ritzmann, D. Hinzke, and U. Nowak, Phys. Rev. B **89**, 024409 (2014).
[28] D. A. Garanin, Phys. Rev. B **55**, 3050 (1997).
[29] O. Chubykalo-Fesenko, U. Nowak, R. W. Chantrell, and D. Garanin, Phys. Rev. B **74**, 094436 (2006).
[30] N. Kazantseva, D. Hinzke, U. Nowak, R. W. Chantrell, U. Atxitia, and O. Chubykalo-Fesenko, Phys. Rev. B **77**, 184428 (2008).
[31] R. F. L. Evans, D. Hinzke, U. Atxitia, U. Nowak, R. W. Chantrell, and O. Chubykalo-Fesenko, Phys. Rev. B **85**, 014433 (2012).
[32] S. Moretti, V. Raposo, and E. Martinez, J. Appl. Phys. **119**, 213902 (2016).
[33] G. Bertotti, *Hysteresis in Magnetism* (Academic Press, San Diego, CA, 1998).
[34] U. Atxitia, O. Chubykalo-Fesenko, N. Kazantseva, D. Hinzke, U. Nowak, and R. W. Chantrell, Appl. Phys. Lett. **91**, 232507 (2007).
[35] E. Martinez, L. Lopez-Diaz, L. Torres, C. Tristan, and O. Alejos, Phys. Rev. B **75**, 174409 (2007).
[36] To be sure that the results are not numerical artifacts we performed simulations for the symmetric cases $d = -2, -4, -6\sigma_L$ obtaining equal results.
[37] If the DW reaches the laser spot, the averaged velocity is obtained as d/t_L, where t_L is the time needed to reach the spot. If the DW does not reach the laser spot, then the velocity is obtained as $d/t_{\max}$, where $t_{\max}$ is the maximum simulation time.
[38] See Supplemental Material at http://link.aps.org/supplemental/10.1103/PhysRevB.95.064419 for movies of the Walker breakdown mechanism and realistic sample depinning.
[39] D. Hinzke, N. Kazantseva, U. Nowak, O. N. Mryasov, P. Asselin, and R. W. Chantrell, Phys. Rev. B **77**, 094407 (2008).
[40] B. Hillebrands and A. Thiaville, *Spin Dynamics in Confined Magnetic Structures III* (Springer, Berlin, 2005).
[41] Δ_0 is calculated by fitting the static Bloch profile, leading to $\Delta_0 = 30$nm. K_S^0 is obtained by calculating the static DW widths (Δ_1, Δ_2) and energies (ϵ_1, ϵ_2) for in-plane and out-of-plane DWs $(\phi_1 = 0,\ \phi_2 = \pi/2)$ and using the relation $K_S^0 = (1 + ab)/a$ [40], with $a = (\Delta_1/\Delta_2)^2$ and $b = (\epsilon_1/\epsilon_2)^2$, leading to $K_S^0 \approx 2.9\times10^5 \mathrm{J/m^3}$.
[42] L. Berger, J. Appl. Phys. **58**, 450 (1985).
[43] D. D. Stancil and A. Prabhakar, in *Spin Waves* (Springer, Boston, 2009), p. 364.